ChemPubSoc Europe

DOI: 10.1002/cctc.201800993

CHEMCATCHEM Full Papers

VIP *Very Important Paper*

Coupling of Nickel Boride and $Ni(OH)_2$ Nanosheets with Hierarchical Interconnected Conductive Porous Structure Synergizes the Oxygen Evolution Reaction

Xiaoguang Liang,[a, b] Ruoting Dong,[a, b] Dapan Li,[a, b] Xiuming Bu,[a, b] Fangzhou Li,[a, b] Lei Shu,[a, b] Renjie Wei,[a, b] and Johnny C. Ho*[a, b, c, d]

Earth-abundant and highly-efficient electrocatalysts for oxygen evolution reaction (OER) are urgently desired to realize the large-scale storage and conversion of renewable energies. In this work, we develop a hierarchical porous electrocatalyst structure utilizing $Ni(OH)_2$ nanosheets directly synthesized on Ni foam as the conductive and interconnected supports. By coupling with amorphous Ni–B nanoparticles, this hybrid catalyst exhibits dramatically enhanced electrocatalytic activities and durabilities towards OER. In specific, along with the optimized Ni–B loading, this catalyst requires only an impressively small overpotential of 300 mV to drive a current density of 100 mA cm^{-2} for oxygen evolution in 1 M KOH electrolyte. Meanwhile, it also yields a small Tafel slope of 49 mV dec^{-1} and a superior long-term stability. All these results evidently indicate that the hierarchical hybridization of Ni–B with $Ni(OH)_2$ on Ni foam can effectively synergize the oxygen evolution, opening up a new vista for designing high-performance transition metal-based nanostructures in the field of electrochemical water splitting.

Introduction

Electrochemical water splitting is a promising large-scale energy storage technique involving the hydrogen evolution reaction (HER) and the oxygen evolution reaction (OER), in which the electrical energy generated from renewable energy sources, such as solar and wind, can be converted to the chemical energy reserved in hydrogen.[1–5] However, this hydrogen production scheme is still mainly hindered by the sluggish kinetics of OER coupled with a 4 electron and 4 proton process, contributing to the significant overpotential loss for water electrolysis.[6–8] In addition to the slow kinetics, the intensive demand of state-of-the-art noble metals and metal oxides based catalysts (e.g., Pt, IrO_2, and RuO_2) for OER is an equally important limitation here due to their intrinsic high costs and poor durability.[9–11] Thus, it is highly desirable to develop highly active, cost-effective and earth-abundant electrocatalysts for OER. In general, emphasis has been first placed on the exploration of nonprecious and efficient transition metal electrocatalysts, including Ni, Co, and Fe-based chalcogenides, phosphides, and nitrides, which exhibit superior electrocatalytic activities in comparison with noble-metal-based catalysts.[12–19] Recently, nickel boride has also been widely reported and made a deep impression by its distinctive OER performance as well as its facile fabrication approach (i.e., dip-coating method), accordingly triggering enormous attention in the research of nickel boride-based electrocatalysts.[20–26]

On the other hand, nanostructured catalysts have been demonstrated as the encouraging alternatives with low costs and excellent performance in water splitting.[27–31] In addition to the large exposed electrode-electrolyte contact area, nanostructures cannot just only enhance the electrolyte penetration and facilitate the release of bubbles attached on the surface of the material, but also provide an excellent charge carrier conduction path with the construction of interconnected networks, resulting in the efficiency improvement of the overall electrochemical process.[27] Nevertheless, these catalytic nanomaterials can be easily peeled off from the surface of working electrodes during the long-term electrochemical operation since their typical drop casting deposition would give the relatively weak adhesion onto the electrode surface. Moreover, the catalytic active sites and the mass diffusion within the working electrode can be substantially deteriorated by using polymer binders such as the polytetrafluoroethylene (PTFE) and Nafion.[20,32] In order to overcome all the above-mentioned issues, direct synthesis of nanostructured materials onto the surface of substrate (e.g., Ni foam) via hydrothermal method can be one of the most simple and flexible approaches, being advantageous to further scale up for industrial applications. In any case, until now, limited success has been obtained to

[a] Dr. X. Liang, R. Dong, D. Li, X. Bu, F. Li, L. Shu, R. Wei, Prof. J. C. Ho
Department of Materials Science and Engineering
City University of Hong Kong
Kowloon Tong, Kowloon (Hong Kong)
E-mail: johnnyho@cityu.edu.hk
[b] Dr. X. Liang, R. Dong, D. Li, X. Bu, F. Li, L. Shu, R. Wei, Prof. J. C. Ho
Shenzhen Research Institute
City University of Hong Kong
Shenzhen 518057 (P.R. China)
[c] Prof. J. C. Ho
State Key Laboratory of Millimeter Waves
City University of Hong Kong
Kowloon Tong, Kowloon (Hong Kong)
[d] Prof. J. C. Ho
Centre for Functional Photonics (CFP)
City University of Hong Kong
Kowloon Tong, Kowloon (Hong Kong)

Supporting information for this article is available on the WWW under https://doi.org/10.1002/cctc.201800993

extend the utilization of high-surface-area nanostructured transition metal-based materials on Ni foam to achieve efficient electrocatalysts because such catalysts still exhibit the insufficient electrocatalytic activity as compared to other material systems.[33,34]

Here, we design and develop a hierarchical electrocatalyst utilizing $Ni(OH)_2$ nanosheets directly synthesized on Ni foam (i.e., $Ni(OH)_2$ @ Ni foam) by a simple hydrothermal technique as the conductive and interconnected supports. By coupling with nickel boride nanoparticles via a facile dip-coating scheme, this hybrid catalyst system is constituted of nickel boride nanoparticles, nickel hydroxide nanosheets and Ni foam (i.e., Ni–B @ $Ni(OH)_2$ @ Ni foam), exhibiting dramatically enhanced electrocatalytic activities and durabilities towards OER. In specific, an overpotential of as low as 300 mV can be impressively achieved with the optimal Ni–B loading to drive the current density of 100 $mA\,cm^{-2}$ in operation. All these results evidently indicate that the hierarchical hybridization of Ni–B with $Ni(OH)_2$ on Ni foam can effectively synergize the oxygen evolution in alkaline media.

Results and Discussion

Figure 1a shows the typical SEM image of Ni foam processed by HCl solution (1 M). By using the hydrothermal method, the nickel hydroxide nanosheets with the thickness of 100 nm were synthesized directly on the surface of Ni foam ($Ni(OH)_2$ @ Ni foam), as illustrated in Figure 1b. It is noted that the surface of Ni foam is covered totally by the $Ni(OH)_2$ nanosheets. Meanwhile, a porous structure was evidently formed on Ni foam through the intersection of $Ni(OH)_2$ nanosheets. Based on this porous structure with the conductively interconnected networks, the nickel boride (Ni–B) nanoparticles were then loaded onto $Ni(OH)_2$ nanosheets (Ni–B @ $Ni(OH)_2$ @ Ni foam) by a simple dip-coating method with different dip-coating cycles of 1, 3, 5 and 7, respectively, as given in Figure 1c to 1f. The fabrication details are also shown in Figure S1 (Supporting Information). For the 1 cycle of dip-coating, it is clear that a large amount of pores are not loaded with the Ni–B nanoparticles, leading to an inhomogeneous deposition of Ni–B onto the $Ni(OH)_2$ nanosheets, as revealed in Figure 1c. This inefficient loading can be attributed to the hindered diffusion of Ni precursor during the dip-coating process induced by the bubbles attached to the $Ni(OH)_2$ nanosheet surface. As increasing of dip-coating to 3 cycles, a homogeneous deposition of Ni–B with high loading rates is obtained, as presented in Figure 1d. With respect to the $Ni(OH)_2$ nanosheets, the top edges and a certain percentage of side edges are still exposed. Figure 1e displays a clear reduced exposure of top and side edges of $Ni(OH)_2$ nanosheets after 5 dip-coating cycles. As compared with the morphology of 3 dip-coating cycles, the $Ni(OH)_2$ nanosheet surface is mainly covered by the small islands which are constituted via the aggregation of Ni–B nanoparticles. These islands can further grow distinctly after 7 dip-coating cycles to cover most of the surface area of $Ni(OH)_2$ nanosheets with less disclosure of their top and side edges, as shown in Figure 1f. All these findings obviously reveal the

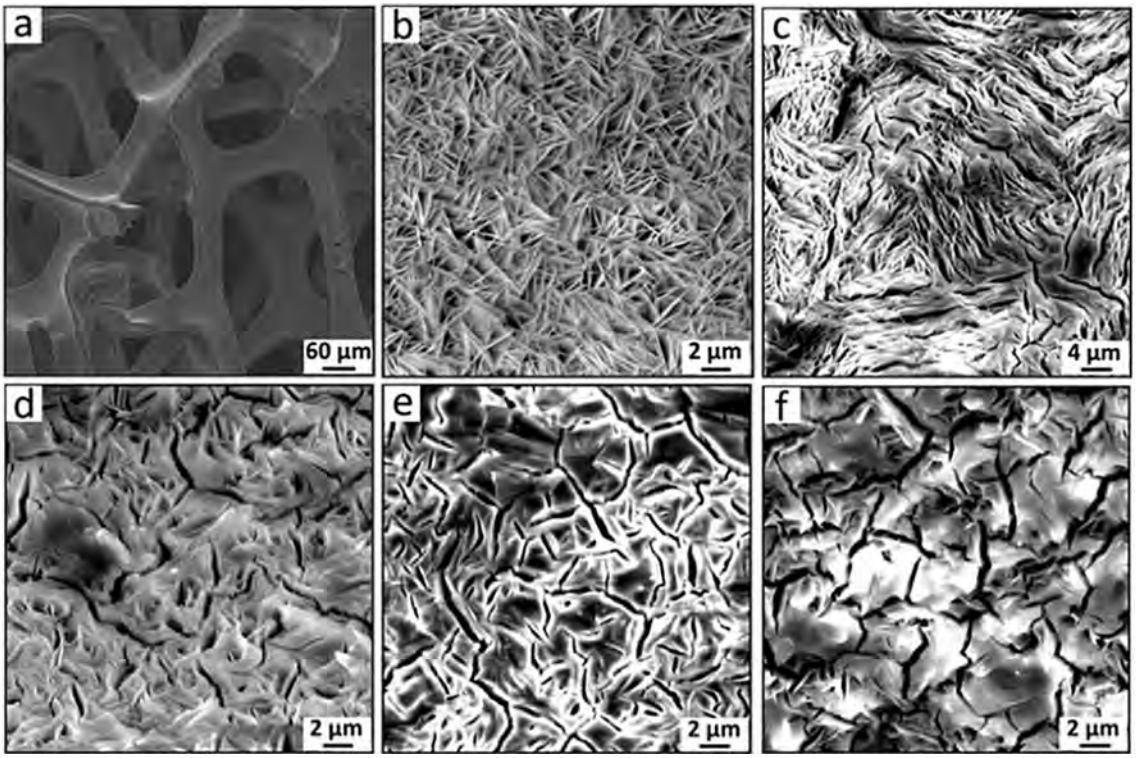

Figure 1. SEM images of (a) Ni foam, (b) $Ni(OH)_2$ nanosheets directly grown on Ni foam by using a facile hydrothermal approach, (c) Ni–B loaded on the $Ni(OH)_2$ nanosheets with 1 dipping cycles, (d) 3 dipping cycles, (e) 5 dipping cycles, (f) 7 dipping cycles.

excellent morphological control of Ni–B @ $Ni(OH)_2$ @ Ni foam by the simple dip-coating fabrication scheme.

Moreover, X-ray diffraction (XRD) and X-ray photoelectron spectroscopy (XPS) are employed to examine the crystal structures and the surface chemical states of as-prepared samples, respectively. Figure 2a illustrates the XRD patterns of Ni foam, $Ni(OH)_2$ @ Ni foam and Ni–B @ $Ni(OH)_2$ @ Ni foam. It is clear that the existence of crystalline $Ni(OH)_2$ can be confirmed by identifying the XRD peaks.[33] In addition, the XPS pattern of starting $Ni(OH)_2$ nanosheets is observed to have a typical peak of 856.2 eV, associating with the Ni 2p3/2 core levels of $Ni(OH)_2$, which indicates the presence of Ni^{2+} phase here, as illustrated in Figure 2b.[11,34,35] Interestingly, as compared with the sample of $Ni(OH)_2$ @ Ni foam, the XRD peaks of Ni–B do not appear, suggesting the amorphous structure of as-prepared Ni–B nanoparticles that is consistent with the previous literatures.[20,21] It is also noted that the amorphous metal-boron-based OER materials usually exhibit an enhanced catalytic efficiency. To demonstrate the formation of amorphous Ni–B nanoparticles synthesized by our dip-coating method, the Ni–B particles are scratched down from Ni foam after 5 dip-coating cycles and tested by XPS. As shown in Figure 2c, the B 1s spectrum of Ni–B nanoparticles yields two distinct peaks at 188.3 and 191.8 eV. The peak at 188.3 eV can be ascribed to the interactions of boron with nickel, while the one at 191.8 eV corresponds to the boron oxide species formed due to the exposure of Ni–B to the ambient.[23] This oxidized species in the composite can facilitate the sluggish OER process because of the deficient boron electron and the sufficient electrons existed in the metal.[23,24] At the same time, Figure 2d displays the two major peaks at 852.7 and 855.9 eV for the Ni 2p spectrum of Ni–B catalysts. The peak at 855.9 eV is attributed to the chemical state of Ni^{2+}, elucidating the existence of nickel oxide or hydroxide species. The peak at 852.7 eV can be assigned to metal nickel constituted in Ni–B catalyst (i.e., Ni^0 2p3/2), which is induced due to the amount and atomic weight of nickel being several times more than that of boron in Ni–B nanoparticles.[21,36] In this case, the reliable formation of Ni–B onto $Ni(OH)_2$ nanosheets via simple dip-coating deposition can be explicitly confirmed with thorough material characterizations.

After that, the OER electrocatalytic activities of as-fabricated electrodes of Ni–B @ $Ni(OH)_2$ @ Ni foam with different dip-coating cycles are investigated in 1 M KOH electrolyte in detail. Before recording the *iR*-corrected linear sweep voltammograms (LSVs), the electrodes are activated by continuous potential cycling at a scan rate of 5 $mV\,s^{-1}$ until stable cyclic voltammograms (CVs) are obtained. According to the LSV polarization curves as depicted in Figure 3a, it is found that the Ni–B @ $Ni(OH)_2$ @ Ni foam exhibits the best electrocatalytic activity after 5 dip-coating cycles with an overpotential of only 300 mV to afford a current density of 100 $mA\,cm^{-2}$ here. This excellent OER activity can be attributed to the optimal amount of Ni–B catalysts loaded onto the $Ni(OH)_2$ nanosheets, as compiled in Table S1 (Supporting information). As compared with the loading weights of 3.37 and 4.9 mg cm^{-2} for the 1 and 3 dip-coating cycles, the loading weight of 7.03 mg cm^{-2} for 5 cycles

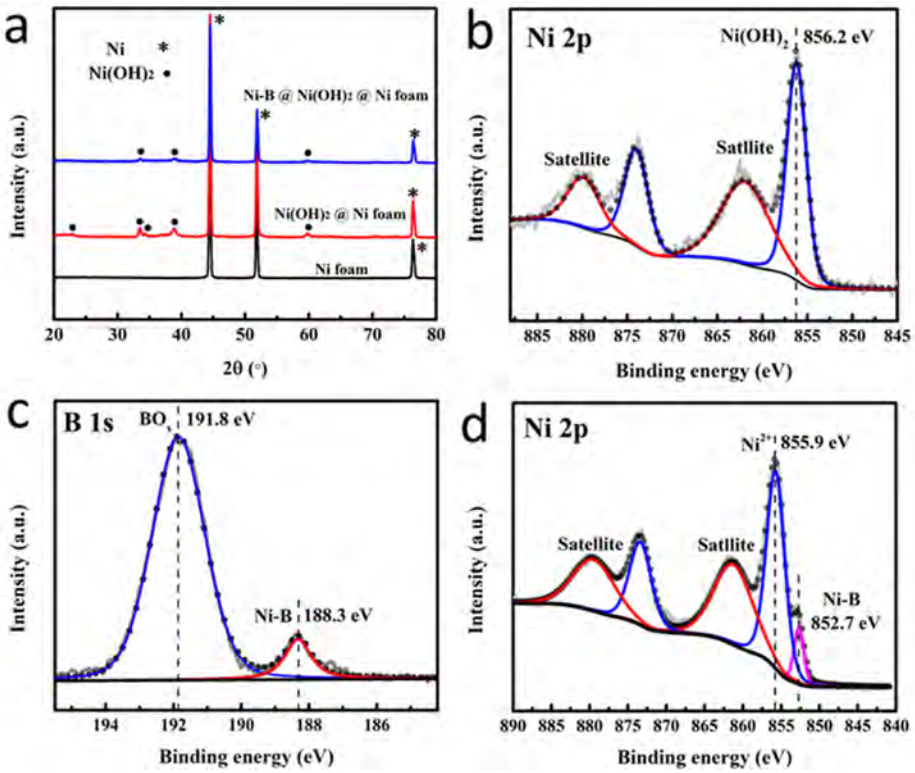

Figure 2. (a) XRD patterns of Ni foam, $Ni(OH)_2$ @ Ni foam, Ni–B @ $Ni(OH)_2$ @ Ni foam. XPS analysis: (b) Ni 2p spectrum of the starting $Ni(OH)_2$ nanosheets, (c) B 1s spectrum and (d) Ni 2p spectrum of Ni–B after the dip-coating deposition.

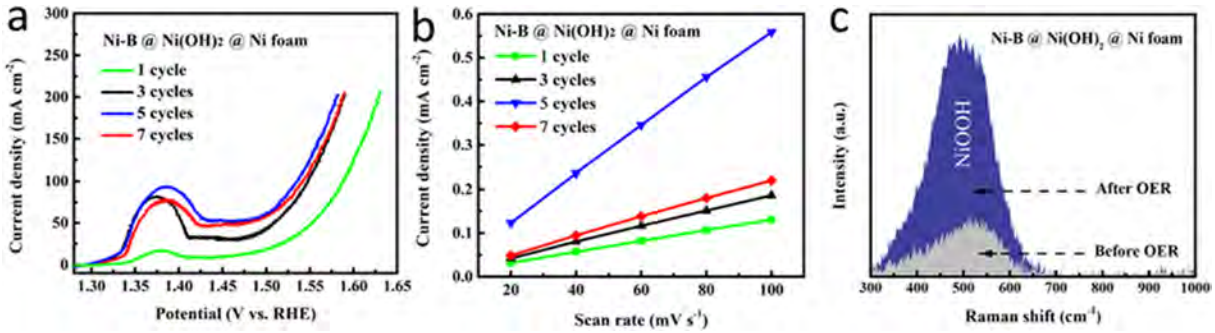

Figure 3. (a) *iR*-corrected LSV curves of Ni–B @ $Ni(OH)_2$ @ Ni foam with different dipping cycles. (b) Current density-scan rate curves of Ni–B @ $Ni(OH)_2$ @ Ni foam with different dipping cycles. (c) Raman spectra of Ni–B @ $Ni(OH)_2$ @ Ni foam before and after OER electrolysis.

indicates more catalytically active sites existed there, which can be deduced from the uniform morphology of Ni–B nanoparticles deposited onto the $Ni(OH)_2$ nanosheets (Figure 1e). However, the electrode made from 7 dip-coating cycles with a loading weight of 7.73 mg cm^{-2} exhibits a slightly higher overpotential of 312 mV for the current density of 100 mA cm^{-2} in comparison with the one of 5 cycles. This OER performance degradation can be ascribed to the formation of big and dense islands on the $Ni(OH)_2$ nanosheet surface (Figure 1f), hindering the penetration of electrolyte and the attendant loss of active sites.

To shed light on the quantity of active sites, the electrochemical double-layer capacitance (C_{dl}), being proportional to the electrochemically active surface area (ECSA), is evaluated in detail by performing cyclic voltammetry at different scan rates (20 – 100 mV s^{-1}) in the non-faradaic processes, as shown in Figure S2.[37,38] In explicit, Figure 3b depicts the linear relationship of the current density against the scan rate, in which the C_{dl} parameter can then be extracted from the calculated slope (Table S2). With the increasing cycles of dip-coating, the C_{dl} value of 5 cycles reaches a maximum of 5.45 mF cm^{-2}, outperforming the C_{dl} value of 1 cycle (1.24 mF cm^{-2}) by ~4.5 times. However, when the dip coating cycle is further increased to 7, the corresponding C_{dl} value becomes 2.15 mF cm^{-2}, indicating the lower catalytically active sites as compared with the one of 5 cycles again due to the formation of dense islands on top of the $Ni(OH)_2$ nanosheets. These results evidently demonstrate that the electrode of Ni–B @ $Ni(OH)_2$ @ Ni foam synthesized via 5 dip-coating cycles possess the superior OER activity because of the synergistic effects contributed from the proper loading weight and the maximized active sites. Additionally, the surface coordination environments of Ni–B @ $Ni(OH)_2$ @ Ni before and after OER electrolysis are also evaluated by Raman spectroscopy. As given in Figure 3c. the relatively weak peak centered at around 530 cm^{-1} can be assigned to the nickel oxide before OER electrolysis owing to the spontaneous oxidization of metal boride in air.[39] After OER operation, it can be seen that a broad peak is obtained, which corresponds to the formation of NiOOH intermediates as the active species facilitating the oxygen evolution process.[20,21] These intermediates are accountable for most of the redox acting for OH^- adsorption in alkaline media.[21]

To confirm the synergistic effect for OER performance enhancement, the LSVs of different electrodes comprising of Ni–B @ Ni foam, $Ni(OH)_2$ @ Ni foam, Ni–B @ $Ni(OH)_2$ @ Ni foam as well as RuO_2 on glassy carbon are acquired under the same testing conditions, as presented in Figure 4a. As anticipated, the $Ni(OH)_2$ @ Ni foam-based electrode affords a high overpotential of 405 mV to drive a current density of 100 mA cm^{-2} because of the scarcity of catalytically active sites of $Ni(OH)_2$ nanosheets, which can be justified by the small C_{dl} value of 0.46 mF cm^{-2} (Figure S3 and Table S2). Despite the active species of NiOOH were also formed on the $Ni(OH)_2$ nanosheet surface during the OER operation (Figure S4), the catalytic activity of

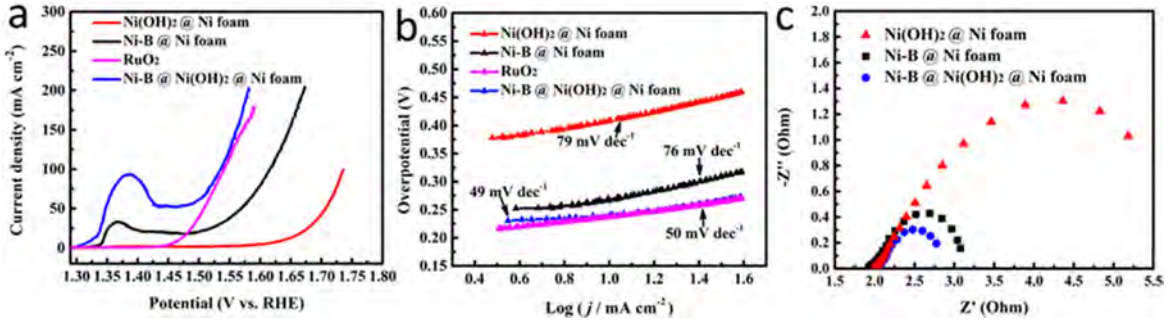

Figure 4. (a) Comparative *iR*-corrected LSVs of Ni–B @ Ni foam (5 dip-coating cycles), $Ni(OH)_2$ @ Ni foam, Ni–B @ $Ni(OH)_2$ @ Ni foam (5 dip-coating cycles) and RuO_2 in 1 M KOH electrolyte, and (b) the corresponding Tafel plots. (c) Nyquist plots of Ni–B @ Ni foam, $Ni(OH)_2$ @ Ni foam, Ni–B @ $Ni(OH)_2$ @ Ni foam as electrodes.

$Ni(OH)_2$ @ Ni foam is still not sufficient for oxygen evolution.[11] In this work, however, the porous hierarchical structure constructed via the intersection of $Ni(OH)_2$ nanosheets onto Ni foam can be utilized as the electrically conducting interconnected networks to support Ni–B nanoparticles, and subsequently forms a synergistic system to enhance the corresponding OER activity. For the electrode without $Ni(OH)_2$ nanosheets (i.e., Ni–B @ Ni foam, 5 dip-coating cycles), it requires an overpotential of 385 mV to drive the current density of 100 mA cm^{-2} due to the lower loading weight (1.03 mg cm^{-2}, Table S1) and the less amount of active sites (C_{dl} = 0.54 mF cm^{-2}, Figure S3 and Table S2) as contrasted with the Ni–B @ $Ni(OH)_2$ @ Ni foam electrode. As compared with the RuO_2 electrode, the Ni–B @ $Ni(OH)_2$ @ Ni foam still presents the better electrocatalytic performance as well as the rapid OER reaction kinetics as confirmed by the smaller values of Tafel slope (Figure 4b). In further evaluating their OER reaction kinetics, electrochemical impedance spectroscopy (EIS) was then employed. As illustrated in the Nyquist plots in Figure 4c, the electrode of Ni–B @ $Ni(OH)_2$ @ Ni foam exhibits the lowest charge transfer resistance as compared with other two Ni foam-based electrodes, indicating that the electrode of Ni–B @ $Ni(OH)_2$ @ Ni foam owns an excellent charge transfer ability during the OER process. It can be attributed to the deposition of Ni–B nanoparticles on these $Ni(OH)_2$ nanosheets with uniform morphology and optimal loading weight, which consequently generates efficient electron transfer pathways throughout the entire Ni–B layer.

Finally, the stability of Ni–B @ $Ni(OH)_2$ @ Ni foam electrode (5 dip-coating cycles) was also assessed in 1 M KOH electrolyte by chronopotentiometry at constant current densities. Figure 5a shows the *iR*-corrected time-dependent overpotential curves measured at the current densities of 50 mA cm^{-2} for 5 h and then 100 mA cm^{-2} for another 5 h, respectively. It is found that there is not any noticeable degradation of overpotential after 10 h of the continuous oxygen generation. Additionally, the LSVs before and after 10 h of chronopotentiometry display the almost identical overpotential at the current density of 100 mA cm^{-2}. More importantly, the SEM image of Ni–B @ $Ni(OH)_2$ @ Ni foam electrode after 10 h testing was also obtained, where there is not any significant change of the surface morphology as given in Figure S5. All these results clearly demonstrate the outstanding stability and durability of Ni–B @ $Ni(OH)_2$ @ Ni foam catalyst for efficient OER in alkaline media.

Conclusions

In summary, even though the poor OER activity of hydrothermally grown $Ni(OH)_2$ nanosheets on Ni foam were typically demonstrated in previous works, we have successfully extended their OER applications by simply utilizing the porous structure formed through the intersection of $Ni(OH)_2$ nanosheets as a support with interconnected conductive networks. By further incorporating amorphous Ni–B nanoparticles into this porous structures via a facile dip-coating method, a hierarchical hybrid electrode consisted of Ni–B nanoparticles, $Ni(OH)_2$ nanosheets and Ni foam (Ni–B @ $Ni(OH)_2$ @ Ni foam, 5 dip-coating cycles) can be readily obtained, which exhibits the superior catalytic activity and stability for oxygen evolution in alkaline media due to the synergistic effects. This work not only provides an earth-abundant electrode configuration with low-cost, large-scale and efficient electrocatalytic activity, but also opens up an avenue to explore the utilization of transition metal-based nanostructures in the field of electrochemical water splitting.

Experimental Section

Chemicals

Hydrochloric acid (HCl, ACS reagent, 37%), isopropyl alcohol (99.7%), ammonium fluoride (NH_4F, ACS reagent, ≥98%), and Nafion solution (5% in a mixture of lower aliphatic alcohols and water) were purchased from Sigma-Aldrich. Potassium hydroxide (KOH, 95%), sodium hydroxide (NaOH, 98%) and urea ($CO(NH_2)_2$, 99%) were bought from Shanghai Meryer Chemical Technology Co. Ltd. Nickel nitrate hexahydrate ($Ni(NO_3)_2{\cdot}6H_2O$, AR, 98%) was acquired from Shanghai Aladdin Bio-chem Technology Co. Ltd. Sodium borohydride ($NaBH_4$, 98%) and nickel (II) chloride hexahydrate ($NiCl_2{\cdot}6H_2O$, 98+%) were obtained from ACROS Organics.

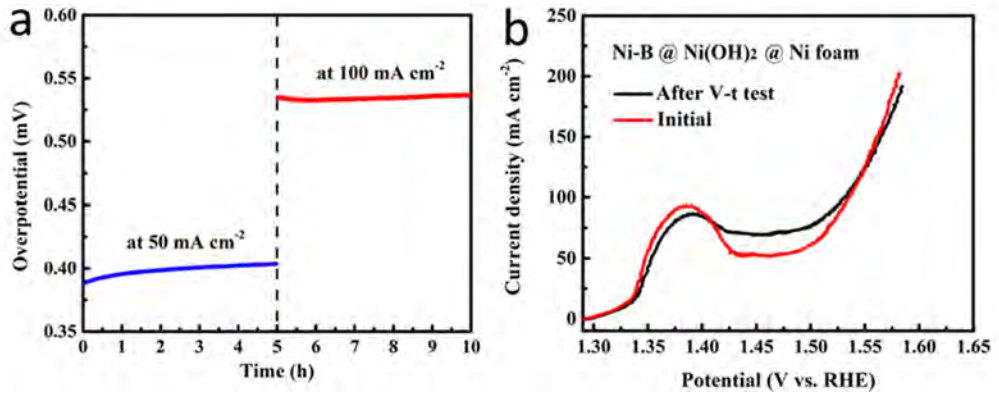

Figure 5. (a) Chronopotentiometric measurements at a current density of 50 mA cm^{-2} for 5 h and another 100 mA cm^{-2} for 5 h. (b) Comparative *iR*-corrected LSV curves before and after the test.

Ruthenium oxide (RuO_2) powder with an average particle size of less than 10 nm was purchased from China Rare Metal Co. Ltd.

Preparation of $Ni(OH)_2$ nanosheets on Ni foam

Ni foam was first cut off into individual sheets with a size of 1× 3 cm and rinsed by ultrasonication in succession with HCl solution (1 M), deionized (DI) water and ethanol for 15 min each, followed by the DI water rinsing and nitrogen gas blow dry. The $Ni(OH)_2$ nanosheets were then directly synthesized on Ni foam by hydrothermal method. In detail, a transparent aqueous solution comprised of 30 mL of DI water, 0.35 g of $Ni(NO_3)_2{\cdot}6H_2O$, 0.09 g of NH_4F and 0.36 g of $CO(NH_2)_2$ was obtained. Next, the aqueous solution and Ni foam were placed inside a Teflon-lined stainless-steel autoclave and maintained at 110 °C for 5 h within an electric oven. The Ni foam coated with $Ni(OH)_2$ nanosheets ($Ni(OH)_2$ @ Ni foam) was eventually taken out from the autoclave after cooling down to room temperature, followed by the alternative rinsing with DI water and ethanol, and then blow dried by nitrogen gas.

Preparation of electrodes

To prepare the hybrid electrode consisting of nickel boride nanoparticles and nickel hydroxide nanosheets on Ni foam (i.e., Ni–B @ $Ni(OH)_2$ @ Ni foam), the nickel precursor solution ($NiCl_2{\cdot}6H_2O$, 20 wt%) and reducing solution ($NaBH_4$, 10 wt% and NaOH, 5 wt%) were obtained separately, and then deaerated with argon flushing for 30 min. By using the dip-coating method, the sample of $Ni(OH)_2$ nanosheets on Ni foam ($Ni(OH)_2$ @ Ni foam) was then dipped into the Ni precursor solution for 15 s, followed by nitrogen gas blow dry and annealing on a hot plate at 50 °C for 10 min. After cooling down to room temperature, the sample was subsequently dipped into the reducing solution for 15 s, followed by the alternative rinsing of DI water and ethanol, and finally blow-dried with nitrogen gas. This dip-coating process was repeated to obtain the electrodes with different process cycles (i.e., 1, 3, 5, and 7 dip-coating cycles). To finish, all samples were dried at 50 °C for 6 h in a vacuum oven. At the same time, the electrode of nickel boride on Ni foam (Ni–B @ Ni foam) was prepared as the control sample with the same procedure as the one of Ni–B @ $Ni(OH)_2$ @ Ni foam. Here, the RuO_2 catalyst prepared on the glassy carbon was also used as a standard electrode for OER. As shown in our previous work, RuO_2 catalyst ink (2 mg mL^{-1}) was obtained by the dispersion of RuO_2 nanoparticles in a mixture of isopropanol alcohol and Nafion (volume ratio 1 to 1). Then, the ink was loaded on the surface of glassy carbon electrode, followed by the drying in air under the radiation of an infrared lamp.

Materials characterizations

Scanning electron microscope (SEM) images were obtained on Quanta FEG450. X-ray diffraction (XRD, SmartLab X-ray diffractometer, Cu Kα radiation, λ = 1.5406 Å) and Raman spectroscopy (Renishaw inVia Raman Microscope) with 532 nm laser beam were used to evaluate the crystal structure of fabricated samples. X-ray photoelectron spectroscopy (XPS) was carried out on a VG Multilab 2000 (Thermo Fisher Scientific, Waltham, MA, U.S.A.) photoelectron spectrometer.

Electrochemical measurements

Electrochemical measurements were performed with a Gamry G300 electrochemical workstation in a standard three-electrode setup under a room temperature of 25 °C. The as-fabricated samples, the saturated calomel electrode (SCE) and platinum (Pt) plate were employed as the working electrode, reference electrode, and counter electrode, respectively. For all electrochemical measurements, 1 M KOH was used as the electrolyte. The cyclic voltammetry (CV) and linear sweeping voltammetry (LSV) scan were measured at a scan rate of 5 mV s^{-1}. The working electrode was activated to be stable before recording by continuous CV scans. In this work, all tested potentials were converted to a reference scale of reversible hydrogen electrode (RHE) by $E_{vs\ RHE} = E_{vs\ SCE} + 0.059 \times PH + 0.242$, where $E_{vs\ SCE}$ is the measured potential referred to the SCE reference electrode. Unless otherwise stated, *iR* compensation provided by the potential station was used to correct all measurements. Electrochemical impedance spectroscopy (EIS) measurements were evaluated with the sweeping of frequency from 100 kHz to 10 mHz. The electrochemical surface area (ECSA) was recorded by the capacitance measurements in a non-faradaic region at scan rates of 20, 40, 60, 80, and 100 mV s^{-1}, accordingly.

Acknowledgements

This work is financially supported by the National Natural Science Foundation of China (Grants 51672229), the Environment and Conservation Fund of Hong Kong SAR, China (ECF 2016–85), the General Research Fund (CityU 11211317) and the Theme-based Research (T42-103/16-N) of the Research Grants Council of Hong Kong SAR, China, and the Science Technology and Innovation Committee of Shenzhen Municipality (Grant JCYJ20170818095520778), and a grant from the Shenzhen Research Institute, City University of Hong Kong.

Conflict of Interest

The authors declare no conflict of interest.

Keywords: oxygen evolution reaction · $Ni(OH)_2$ nanosheets · Ni–B nanoparticles · hierarchical hybridization · synergistic effects

[1] W. Gao, Z. Xia, F. Cao, J. C. Ho, Z. Jiang, Y. Qu *Adv. Funct. Mater.* **2018**, *28*, 1706056.
[2] R. Wei, X. Zhou, T. Zhou, J. Hu, J. C. Ho *J. Phys. Chem. C.* **2017**, *121*, 19002–19009.
[3] S. Czioska, J. Wang, S. Zuo, X. Teng, Z. Chen *ChemCatChem.* **2018**, *10*, 1005–1011..
[4] G. Dong, M. Fang, J. Zhang, R. Wei, L. Shu, X. Liang, S. Yip, F. Wang, L. Guan, Z. Zheng, J. C. Ho *J. Mater. Chem. A.* **2017**, *5*, 11009–11015.
[5] J. Chen, Y. Li, G. Sheng, L. Xu, H. Ye, X. Z. Fu, R. Sun, C. P. Wong *ChemCatChem.* **2018**, *10*, 2248–2253.
[6] N. T. Suen, S. F. Hung, Q. Quan, N. Zhang, Y. J. Xu, H. M. Chen *Chem. Soc. Rev.* **2017**, *46*, 337–365.
[7] Z. W. Seh, J. Kibsgaard, C. F. Dickens, I. Chorkendorff, J. K. Norskov, T. F. Jaramillo *Science.* **2017**, *355*.
[8] M. Gong, D. Y. Wang, C. C. Chen, B. J. Hwang, H. Dai *Nano Res.* **2015**, *9*, 28–46.
[9] P. Wang, Z. Pu, Y. Li, L. Wu, Z. Tu, M. Jiang, Z. Kou, I. S. Amiinu, S. Mu *ACS Appl. Mater. Interfaces.* **2017**, 9, 26001–26007.
[10] Z. Pu, Y. Xue, W. Li, I. S. Amiinu, S. Mu *New J. Chem.* **2017**, 41, 2154–2159.
[11] A. Eftekhari *Materials Today Energy.* **2017**, *5*, 37–57.
[12] M. Fang, W. Gao, G. Dong, Z. Xia, S. Yip, Y. Qin, Y. Qu, J. C. Ho *Nano Energy.* **2016**, *27*, 247–254.

[13] S. Klaus, Y. Cai, M. W. Louie, L. Trotochaud, A. T. Bell *J. Phys. Chem. C.* **2015**, *119*, 7243–7254.
[14] J. Liu, C. Liu, Y. Wan, W. Liu, Z. Ma, S. Ji, J. Wang, Y. Zhou, P. Hodgson, Y. Li *CrystEngComm.* **2013**, *15*, 1578.
[15] L. Huang, D. Chen, Y. Ding, S. Feng, Z. L. Wang, M. Liu *Nano Lett.* **2013**, *13*, 3135–3139.
[16] S. Peng, L. Li, H. B. Wu, S. Madhavi, X. W. D. Lou *Adv. Energy Mater.* **2015**, *5*, 1401172.
[17] C. Tang, N. Cheng, Z. Pu, W. Xing, X. Sun *Angew. Chem. Int. Ed. Engl.* **2015**, *54*, 9351–9355.
[18] L. A. Stern, L. Feng, F. Song, X. Hu *Energy Environ. Sci.* **2015**, *8*, 2347–2351.
[19] X. Zhu, T. Jin, C. Tian, C. Lu, X. Liu, M. Zeng, X. Zhuang, S. Yang, L. He, H. Liu, S. Dai *Adv. Mater.* **2017**, 1704091.
[20] L. Trotochaud, S. L. Young, J. K. Ranney, S. W. Boettcher *J. Am. Chem. Soc.* **2014**, *136*, 6744–6753.
[21] H. -Y. Wang, Y. -Y. Hsu, R. Chen, T. -S. Chan, H. M. Chen, B. Liu R *Adv. Energy Mater.* **2015**, *5*, 1500091.
[22] J. Jiang, M. Wang, W. Yan, X. Liu, J. Liu, J. Yang, L. Sun *Nano Energy.* **2017**, *38*, 175–184.
[23] Y. Liang, X. Sun, A. M. Asiri, Y. He *Nanotechnology.* **2016**, *27*, 12LT01.
[24] M. Arivu, J. Masud, S. Umapathi, M. Nath *Electrochem. Commun.* **2018**, *86*, 121–125.
[25] J. M. V. Nsanzimana, Y. Peng, Y. Y. Xu, L. Thia, C. Wang, B. Y. Xia, X. Wang *Adv. Energy Mater.* **2017**, 1701475.
[26] J. Masa, I. Sinev, H. Mistry, E. Ventosa, M. de la Mata, J. Arbiol, M. Muhler, B. Roldan Cuenya, W. Schuhmann *Adv. Energy Mater.* **2017**, 1700381.
[27] H. Li, P. Wen, Q. Li, C. Dun, J. Xing, C. Lu, S. Adhikari, L. Jiang, D. L. Carroll, S. M. Geyer *Adv. Energy Mater.* **2017**, *7*, 1700513.
[28] W. J. Jiang, S. Niu, T. Tang, Q. H. Zhang, X. Z. Liu, Y. Zhang, Y. Y. Chen, J. H. Li, L. Gu, L. J. Wan, J. S. Hu *Angew. Chem. Int. Ed. Engl.* **2017**, *56*, 6572–6577.
[29] M. Fang, G. Dong, R. Wei, J. C. Ho *Adv. Energy Mater.* **2017**, 1700559.
[30] Q. Wei, F. Xiong, S. Tan, L. Huang, E. H. Lan, B. Dunn, L. Mai *Adv. Mater.* **2017**, *29*.
[31] C. H. Lu, M. H. Hon, I. C. Leu *J. Electron. Mater.* **2016**, *46*, 2080–2084.
[32] B. I. Kharisov, O. V. Kharissova, B. O. García, Y. P. Méndez, I. G. de la Fuente *RSC Adv.* **2015**, *5*, 105507–105523.
[33] D. Kong, J. Luo, Y. Wang, W. Ren, T. Yu, Y. Luo, Y. Yang, C. Cheng *Adv. Funct. Mater.* **2014**, *24*, 3815–3826.
[34] I. S. Amiinu, Z. Pu, D. He, H. G. R. Monestel, S. Mu *Carbon.* **2018**, 137, 274–281.
[35] P. Chen, K. Xu, Z. Fang, Y. Tong, J. Wu, X. Lu, X. Peng, H. Ding, C. Wu, Y. Xie *Angew. Chem.* **2015**, *127*, 14923–14927; *Angew. Chem. Int. Ed.* **2015**, *54*, 14710–14714.
[36] M. Gao, W. Sheng, Z. Zhuang, Q. Fang, S. Gu, J. Jiang, Y. Yan *J. Am. Chem. Soc.* **2014**, *136*, 7077–7084.
[37] X. Zhou, Z. Xia, Z. Zhang, Y. Ma, Y. Qu *J. Mater. Chem. A.* **2014**, *2*, 11799–11806.
[38] J. Ji, L. L. Zhang, H. Ji, Y. Li, X. Zhao, X. Bai, X. Fan, F. Zhang, R. S. Ruoff *ACS Nano.* **2013**, *7*, 6237–6243.
[39] H. Li, H. Li, W.-L. Dai, W. Wang, Z. Fang, J.-F. Deng *Appl. Surf. Sci.* **1999**, *152*, 25–34.
[40] T. Tang, W. J. Jiang, S. Niu, N. Liu, H. Luo, Y. Y. Chen, S. F. Jin, F. Gao, L. J. Wan, J. S. Hu *J. Am. Chem. Soc.* **2017**, *139*, 8320–8328.
[41] C. Z. Yuan, Y. F. Jiang, Z. Wang, X. Xie, Z. K. Yang, A. B. Yousaf, A. W. Xu *J. Mater. Chem. A.* **2016**, *4*, 8155–8160.
[42] C. Liu, C. Li, K. Ahmed, Z. Mutlu, C. S. Ozkan, M. Ozkan *Sci. Rep.* **2016**, *6*, 29183.

Manuscript received: June 20, 2018
Accepted Article published: August 19, 2018
Version of record online: September 13, 2018